Cyclic quenching treatment doubles the Charpy V-notch impact energy of a 2.3 GPa maraging steel

Zhou, Xinlei; Jia, Chunni; Mi, Peng; Zhang, Honglin; Yan, Wei; Wang, Wei; Sun, Mingyue; van der Zwaag, Sybrand; Rong, Lijian

DOI
10.1016/j.jmst.2024.05.026

Publication date
2025

Document Version
Final published version

Published in
Journal of Materials Science and Technology

Journal of Materials Science & Technology 209 (2025) 311–328

Contents lists available at ScienceDirect

Journal of Materials Science & Technology

journal homepage: www.elsevier.com/locate/jmst

Research Article

Cyclic quenching treatment doubles the Charpy V-notch impact energy of a 2.3 GPa maraging steel

Xinlei Zhou[a,b], Chunni Jia[b], Peng Mi[c], Honglin Zhang[b], Wei Yan[b,*], Wei Wang[b], Mingyue Sun[b], Sybrand van der Zwaag[d], Lijian Rong[b,*]

[a] School of Materials Science and Engineering, University of Science and Technology of China, Shenyang 110016, PR China
[b] Shi-changxu Innovation Center for Advanced Materials, Institute of Metal Research, Chinese Academy of Sciences, Shenyang 110016, PR China
[c] China Aerodynamics Research and Development Center, Mianyang 621000, PR China
[d] Faculty of Aerospace Engineering, Delft University of Technology, Delft, Netherlands

ARTICLE INFO

Article history:
Received 7 April 2024
Revised 7 May 2024
Accepted 26 May 2024
Available online 31 May 2024

Keywords:
Maraging steel
Cyclic quenching treatment
Ni partitioning
Ultrafine lath
Austenite
Toughness

ABSTRACT

A cyclic quenching treatment (CQT) succeeded in turning a 2.3 GPa maraging steel with a Charpy impact energy of 9 J into a new grade with the same strength but a Charpy impact energy of 20 J upon 4 cyclic treatments. The improvement of mechanical properties is attributed to the refinement and increased chemical heterogeneity of the martensitic substructure, rather than the refinement of prior austenite grain (PAG), as well as the Transformation-Induced Plasticity (TRIP) effect facilitated by small austenite grains. The role of local segregation of Ni during CQT in the formation of Ni-rich austenite grains, Ni-rich martensite laths and Ni-poor martensite laths, was investigated and verified by DICTRA simulations. This study highlights the important influence of Ni partitioning behavior during CQT, providing insights into microstructural evolution and mechanical properties.

1. Introduction

Owing to their superior mechanical and corrosive properties, ultra-high strength (maraging) steels (UHSSs) have been applied for some decades to construct system-critical components such as piston rods, aircraft landing gears, missile shells, sophisticated balances for strain measurement in wind tunnels, and so on [1–4]. However, in order to guarantee a safe operation under unexpected conditions, such as transient overloads, not only a high strength but also a high toughness is required. It has been known for a long time that for most metallic systems compositional and processing changes made to increase the tensile strength generally also result in a toughness reduction [5–7]. For the UHSSs family to be addressed in this work when the strength is higher than 2.1 GPa, the room temperature (RT) Charpy V-notch impact energy is rarely over 15 J [8,9].

Grain refinement has been recognized as the only effective way of improving strength and toughness simultaneously. Such grain refinement can be achieved by controlling the grain nucleation and growth behavior during recrystallization or by controlling the kinetics of solid-state phase transformations [10,11]. The thermal-mechanical control processing (TMCP) method has been used very successfully in the development of high strength low alloy steels such as pipeline steels to reduce the prior austenite grain (PAG) during hot rolling size from usually 30 μm to below 5 μm remarkably promoting both strength and toughness, resulting in a big scientific and commercial breakthrough for high strength low alloy (HSLA) steels [12,13]. While TMCP is a potential route for structures refinement and properties enhancement, it is generally unsuitable for maraging steels because of a lack of recrystallization barriers like NbC carbides due to the super low carbon content, usually under 0.005 %. Even so, Luo et al. [14] have managed to refine the PAG size to around 6 μm and get refined martensite substructures by suitable hot rolling.

While being a complex and costly heat treatment process, the cyclic quenching treatment (CQT) has also been applied to maraging steels to refine their PAG, since the newborn grains are getting smaller during successive heating and quenching cycles [15–18]. The CQT includes multiple successive treatments involving a fast-heating step to temperatures just above the phase transformation temperatures, Ac_1 or Ac_3, a short time holding to let newborn austenite grains develop, and a quenching step to stop the further growth of such small grains. Nakazawa et al. [16] have applied the CQT, consisting of multiple cycles of heating to inter-critical

* Corresponding authors.
E-mail addresses: weiyan@imr.ac.cn (W. Yan), ljrong@imr.ac.cn (L. Rong).

https://doi.org/10.1016/j.jmst.2024.05.026
1005-0302/

temperatures (between Ac_1 and Ac_3) followed by water quenching, to refine the PAG of a high-strength maraging steel to 10 μm, and to obtain a superior ductility while maintaining high strength. Saha et al. [17] reported that the PAG of a carbon steel was refined from 147 to 7 μm by an 8-cycle CQT with short-duration holding at a temperature above the Ac_3 temperature and air cooling. The refined microstructure exhibited an excellent combination of strength and toughness. In addition, Hou et al. [19] have reported for a low carbon precipitation-strengthened steel that CQT could result in a great reduction of effective grain size (EGS) defined as the size of grains surrounded by high angle boundaries (HABs, misorientation angle greater than 15°) so as to greatly improve toughness [20–22]. Irrespective of whether the PAG or the EGS was taken as the critical microstructural parameter responsible for the improvement in Charpy V-notch impact toughness, the changes are attributed to the change in their dimension, rather than to any changes in local composition, due to (incomplete) element partitioning during the austenite formation.

In the present work, the CQT has been explored with the initial aim to reduce the PAG size of a 2.3 GPa ultra-high strength maraging steel so as to improve the RT Charpy V-notch impact energy. The study of the mechanical properties as a function of the number of CQT cycles was complemented by detailed microstructural studies in which not only the changes in PAG and EGS were determined but also the changes in the chemical composition of the austenite grains and the surrounding martensitic matrix.

2. . Experimental

2.1. Materials preparation

The experimental 2.3 GPa maraging steel was melted in a 200 kg vacuum induction furnace, cast, scalped and vacuum arc remelted. The final chemical composition is shown in Table 1. The ingot was soaked at 1250 °C for 12 h, forged into rods with 30 mm in diameter, and then air cooled to RT. Samples for CQT with the dimensions of 11 mm × 11 mm × 60 mm were cut out of the forged rods.

Table 1
Chemical composition of the 2.3 GPa maraging steel (wt.%).

Fe	Ni	Co	Mo	Ti	C
Bal.	17.3	11.5	5.3	1.0	0.003

The typical phase transformation points, such as the austenite transformation starting temperature (Ac_1), finishing temperature (Ac_3), and martensite start (Ms) temperature, required to set the conditions for the CQT were determined by dilatometry using a heating rate of 10 °C/s and a cooling rate of 5 °C/s. The Ac_1, Ac_3, and Ms temperatures were found to be 680, 800, and 220 °C, respectively, as shown in Fig. 1(a). To prepare the initial basic microstructure before the CQT, all samples were soaked at 850 °C for 1 h, water cooled to RT, and stored in liquid nitrogen for 8 h to get a fully martensitic microstructure. Sample A was directly subjected to aging treatment at 500 °C for 3 h after the cryogenic treatment, as shown in Fig. 1(b), to create a reference state against which to evaluate the effect of the CQT. Instead of direct aging, the CQT samples were re-heated to the soaking temperature of 850 °C again over a period of 2 h (7200 s) and held for a short time of 15 min, and then water quenched to RT. The samples were labeled as B1–B7, according to the number of CQT cycles (1 till 7 cycles) respectively. Finally, all CQT samples B1–B7 were aged at 500 °C for 3 h. The above heat treatment process is shown in Fig. 1(c). No cryogenic treatment was imposed on the samples B1–B7.

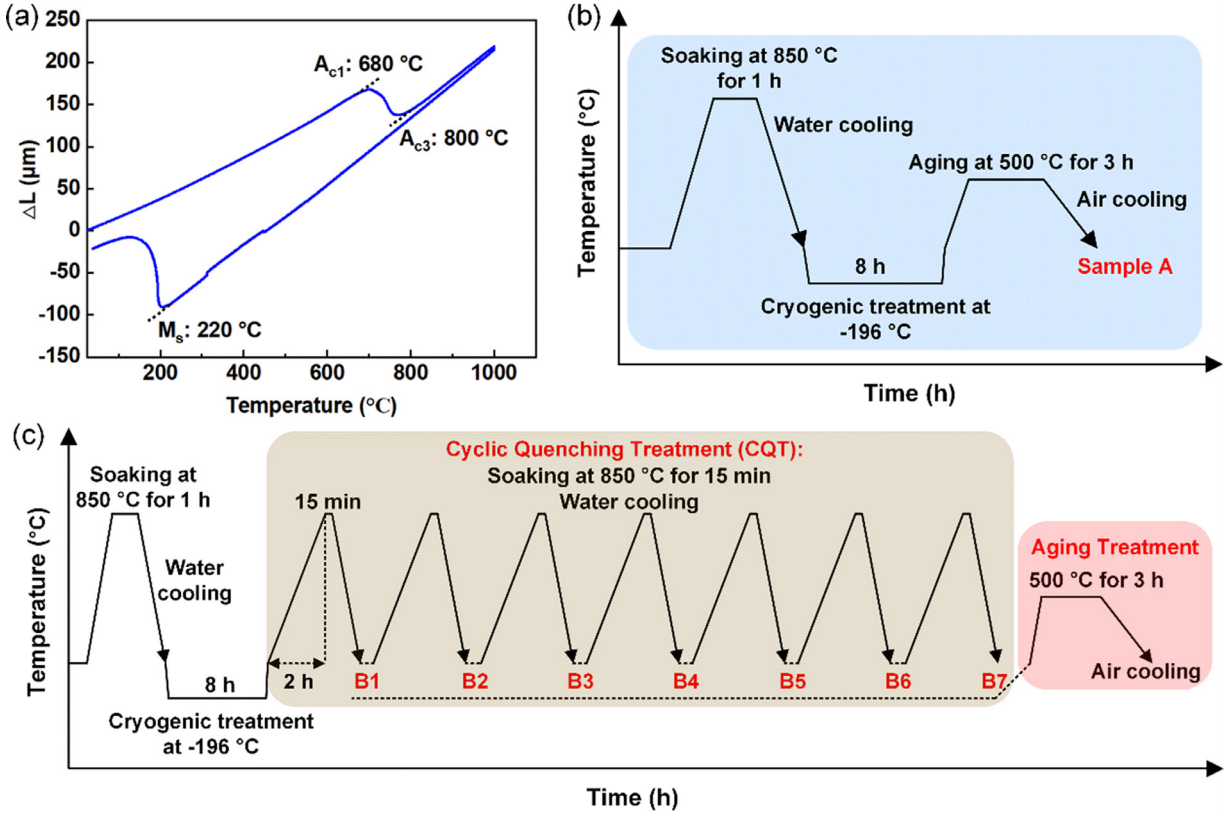

Fig. 1. (a) Typical phase transformation points of the experiment steel, (b) heat treatment process of sample A, (c) heat treatment process of the samples B1–B7.

2.2. Mechanical property testing

Tensile tests were carried out on a TSE504D testing machine. Tensile samples were 5 mm in diameter and had a gauge length of 25 mm. The RT Charpy impact tests were conducted on a ZBC2452-C pendulum impact testing machine. The dimension of the standard Charpy V-notch impact samples was 10 mm × 10 mm × 55 mm. At least three samples were tested to get an average value. The scatter in Charpy impact energy per condition is typically around 0.5 J.

2.3. Microstructure analysis

Samples with different numbers of CQT cycles were etched in the solution of 5 g picric acid plus 100 mL water at 80 °C for 60 s to reveal the PAG size (measured as Equivalent circle diameter) under an optical microscope. The average values of PAG size were determined from measurements covering 30 grains.

The austenite volume fraction, the morphologies of austenite grains such as size, shape, and spatial distribution, are all important factors affecting the strength and toughness, especially in such ultra-high strength maraging steels. Additionally, the misorientation angles between the substructure units are also critical to the strength and toughness. So, electron back-scattered diffraction (EBSD) was employed to characterize both the morphology of the austenite and the changes in the martensite substructure boundaries in the heat-treated samples described above. The samples for EBSD tests were electrolytically polished in the mixed solution with 7 vol.% $HClO_4$ and 93 vol.% ethanol at 30 V for 70 s at −25 °C. Diffraction patterns were collected using Gemini 300 scanning electron microscopy (SEM) with an acceleration voltage of 20 kV. The EBSD raw dates were analyzed using the HKL-Channel 5 software.

As the martensite laths have dimensions of the order of nanometers, they cannot be identified in conventional EBSD. Hence the transmission Kikuchi diffraction (TKD) with a higher acceleration voltage was used to identify any changes in the martensite laths [23]. Samples for TKD were prepared via twin-jet polishing using an electrolyte containing 10 vol.% $HClO_4$ and 90 vol.% ethanol at −25 °C and a voltage of 27 V. TKD analysis was carried out using a ZEISS Gemini at 30 kV with a scanning step size of 6 nm.

The dilatation curves can provide information on austenite formation and elemental partitioning during CQT, which helps to explain the obtained microstructures in the B1−B7 grades. The dilation experiments were conducted on a L78RITA dilatometer using one sample with dimensions of 3 mm in diameter and 10 mm in length imposing several CQT treatments in the same manner as the bulk material. The experimental procedure consisted of heating to 850 °C with a heating rate of 0.1 °C/s, held for 15 min, followed by a cooling rate of 100 °C/s to RT.

The employed ultra-high strength maraging steel in the present research is strengthened by nanosized Mo-enriched, Ni_3Ti precipitates that are present after aging treatment. To detect any changes that the CQT treatment may induce in these nanoparticles and their interaction with dislocations, these precipitates were observed using transmission electron microscopy (TEM) and atom probe tomography (APT). The TEM observations were made on an FEI Talos F200x field emission TEM operated at 200 kV. Needle-shaped specimens for APT were lifted out and annular milled in an FEI Scios focused ion beam/scanning electron microscope (FIB/SEM). The APT characterizations were performed in a local electrode atom probe (Cameaca Leap 5000 XR). The data analysis workstations AP Suite 6.1 was adopted to create the 3D reconstructions.

3. Results

3.1. . Mechanical properties

Sample A, subjected to a direct aging treatment after the cryogenic treatment, possesses an ultimate tensile strength (UTS) of 2288 MPa and yield strength (YS) of 2112 MPa, respectively, as shown in Fig. 2(a). However, the RT Charpy V-notch impact energy of sample A is only 9 J, as shown in Fig. 2(b). The strength of sample B1 is the same as sample A, but the RT Charpy impact energy slightly increases to 12 J. However, the RT Charpy impact energy of sample B4 has increased to an average of 22.5 J, 2.5 times that of sample A, even without any loss in UTS. The observation shows that the CQT has successfully improved the RT Charpy impact energy of the high strength maraging steel. However, when the number of CQT cycles is over 4, the UTS level drops only gradually while the YS of samples B6 and B7 dropped to 1848 and 1798 MPa, respectively, although the RT Charpy V-notch impact energy remains greater than 20 J and even increases slightly with the number of CQT cycles. The tensile stress–strain curves of the sample A, B1, B4, B6 and B7 are presented in Fig. 2(c) and elongation of sample B1−B7 is shown in Table S1 in supplementary materials. It can be observed that the elongation of the samples remains constant with the increase in the number of CQT cycles.

In order to compare the mechanical properties of the samples with different number of CQT cycles with those of high-strength steels that have already been engineered, a map of Charpy V-notch impact energy versus YS is shown in Fig. 2(d). In comparison to existing steels with a YS exceeding 1500 MPa, the CQT treated samples, in particular sample B4, exhibit an excellent combination of Charpy V-notch impact energy and strength.

3.2. Microstructures

3.2.1. The PAG size as a function of the number of CQT cycles

Fig. 3 shows the microstructure of the set of sample A, sample B1, sample B4, and sample B6 examined prepared to reveal the PAG. Somewhat unexpectedly, the results clearly show that the PAG does not change by the application of CQT cycles. The PAG sizes as determined by conventional quantitative metallurgy methods are also listed in Table 2 and confirm the constancy of the PAG size.

3.2.2. Microstructure without CQT

Sample A, which is not subjected to a CQT, can be seen as a microstructural counterpart of samples which were exposed to a CQT. As shown in Fig. 4(a), sample A exhibits a normal martensitic microstructure. The XRD pattern in Fig. 4(b) proves that almost no austenite is present. It can be seen in the EBSD image that the martensitic microstructure of sample A is a typical hierarchical substructure including packets and blocks whose boundaries are HABs, as is shown in the inverse pole figure (IPF) map with HABs (black lines) in Fig. 4(c). The average width of the packets and blocks is 50 and 20 μm, respectively. The observation from bright-field TEM (BF-TEM) shown in Fig. 4(d) reveals that the matrix is composed of martensite laths with an average width of 500 nm.

3.2.3. Microstructural changes because of CQT

3.2.3.1. Austenite grains in the CQT samples. The spatial distribution of the austenite grains in the samples with different numbers of CQT cycles is displayed in Fig. 5, where the small austenite grains are marked in red and the martensite is marked in blue based on an analysis using the band-contrast (BC) mode, respectively. In general, the volume fraction of austenite increases with the number of CQT cycles. Namely, the volume fraction of the austenite is

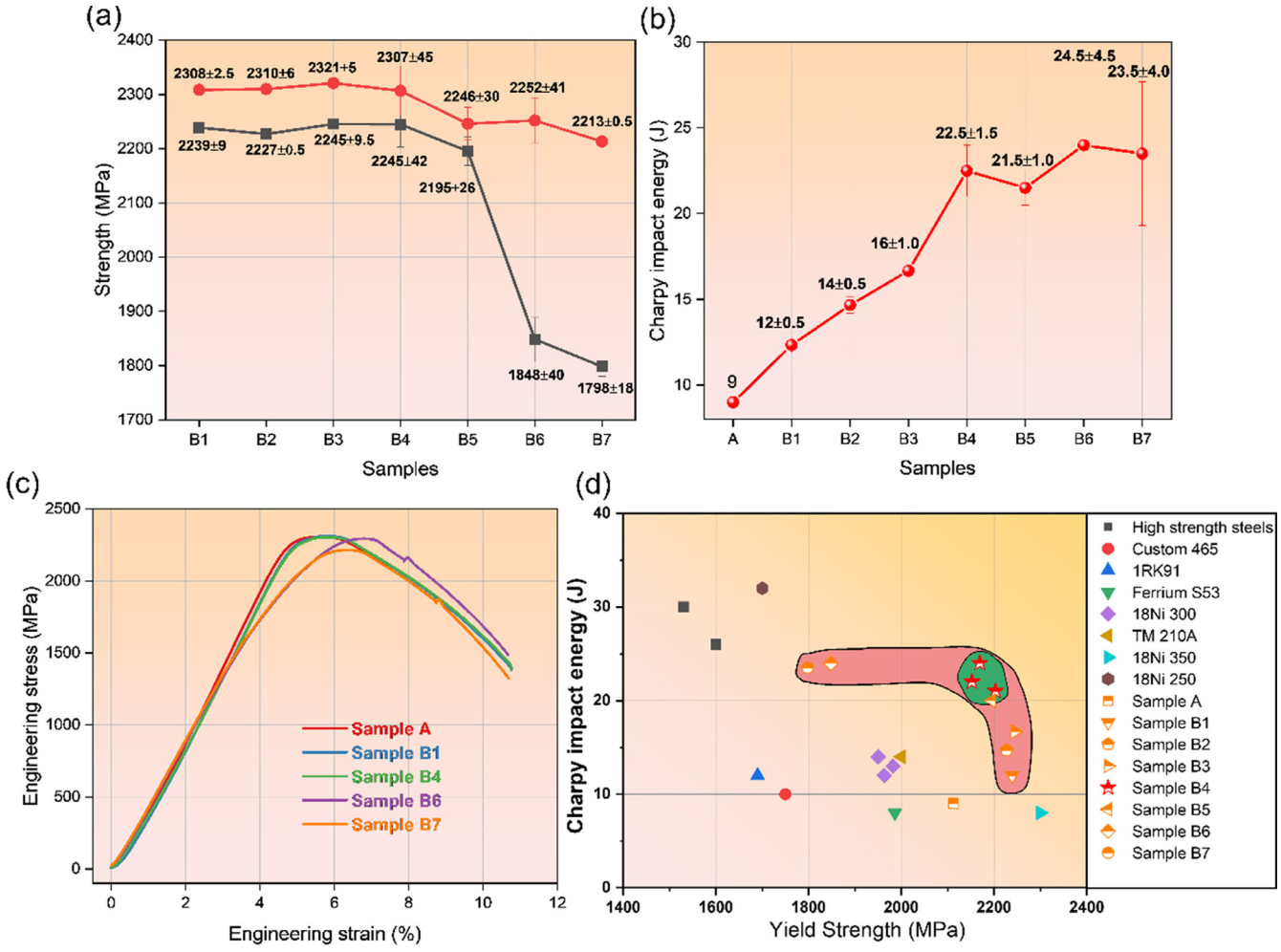

Fig. 2. (a) Ultimate tensile strength, yield strength of sample A and sample B1–B7; (b) Charpy V-notch impact energy at RT of sample A and sample B1–B7; (c) tensile stress–strain curves of sample A, B1, B4, B6 and B7; (d) map of Charpy V-notch impact energy versus yield strength at RT of sample A, sample B1–B7 and selected commercial high strength steels [24] including Custom 465, 1RK91, Ferrium S53 [25], TM210A, 18Ni 250, 18Ni 300 [26], and 18Ni 350.

Table 2
The PAG size of samples with different numbers of CQT cycles (μm).

Sample A	B1	B2	B3	B4	B5	B6	B7
190 ± 44	213 ± 41	201 ± 38	220 ± 39	219 ± 51	207 ± 41	214 ± 32	228 ± 45

revealed to be 1.36 % in sample B1, 4.91 % in sample B3, 6.59 % in sample B4, and 14.45 % in sample B6 according to the phase maps. When the number of CQT cycles exceeds 4, as shown in Fig. 5(d, e) (sample B4 and sample B6), the distribution of small blocky austenite grains becomes much more uniform.

The TEM morphology of the small austenite grains in the samples with different numbers of CQT cycles is shown in Fig. 6. On the whole, the size of the austenite grains gradually increased with the cycle number. Some blocky austenite grains with an average length of 50 nm are found in sample B1, as shown in Fig. 6(a). The corresponding SAED pattern oriented at $[110]_{\gamma}$ zone axis reveals that the orientation between the austenite grains and martensitic matrix follows the Kurdyumov–Sachs (K–S) relationship. In sample B2, larger austenite grains with a length of about 1 μm and a width of 200 nm are observed. In addition to the large austenite grains, some small austenite grains with the same size as that in sample B1 are also observed, as shown in Fig. 6(b). In the case of four CQT cycles, blocky austenite grains (marked by A2 in Fig. 6(c)) with a length of 500 nm are observed in the matrix. Besides, just as in sample B2, some small austenite grains of around 50 nm were also found in sample B4, as marked by A1, illustrating that new small austenite grains are being formed at every CQT cycle. When the number of cycles exceeded six (sample B6), the length of blocky austenite often surpassed a value of 2 μm (marked by A3), as shown in Fig. 6(d).

The atomic concentration (at.%) of Ni in the austenite grains of samples B1, B2 and B4 are obtained from the EDS point-scanning analysis under the annular bright-field scanning TEM (ABF-STEM) mode, as shown in Fig. 6(f). The four points are taken from each sample for measurement. The Ni content in those austenite grains is higher than that in the nominal composition of the steel, indicating that the formation of such austenite grains is related to Ni partitioning. Furthermore, the Ni content in the austenite grains increases with an increasing number of CQT cycles. The austenite grains in sample B4 are identified to have a Ni content of 24.65 %, higher than that in sample B2 (19.97 %), and sample B1 (18.88 %). The average contents of alloying elements in the austenite grains of the samples with different numbers of CQT cycles were ana-

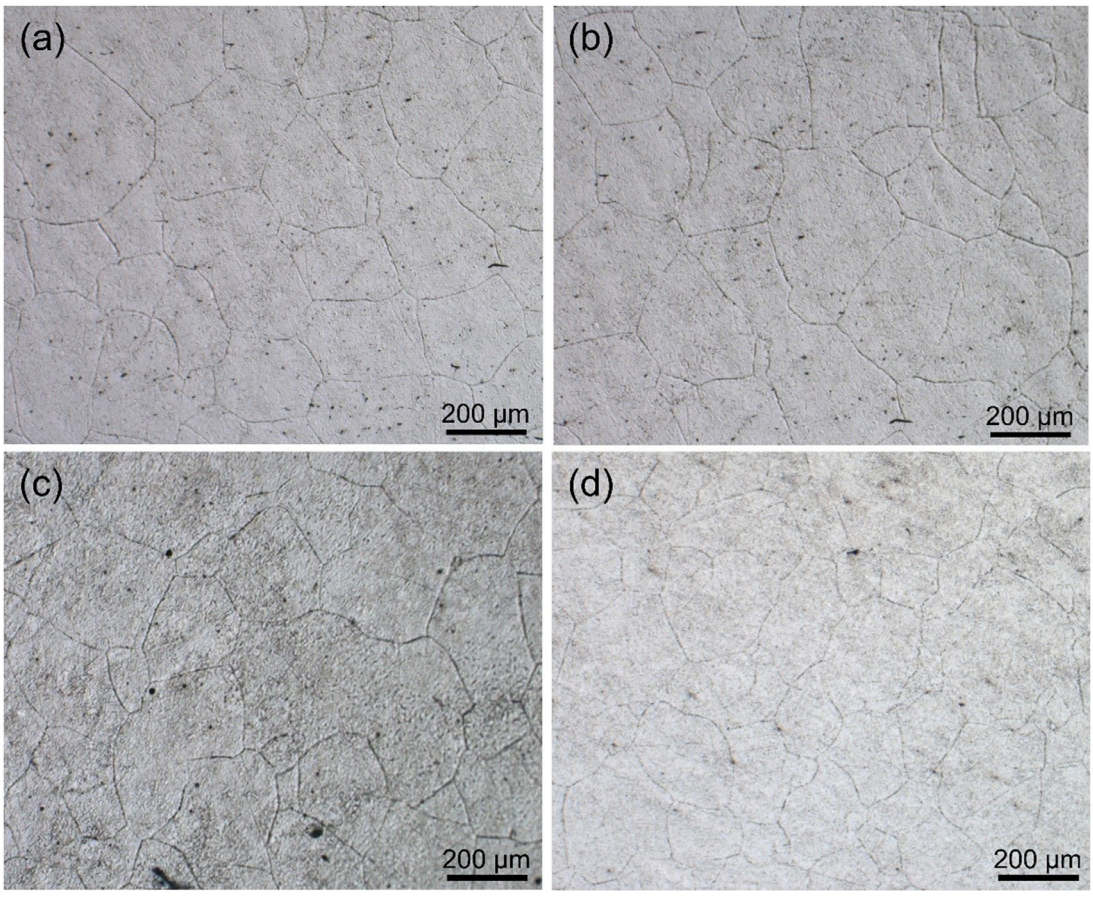

Fig 3. Optical micrographs of the (a) sample A, (b) sample B1, (c) sample B4, (d) sample B6 etched to reveal the PAG.

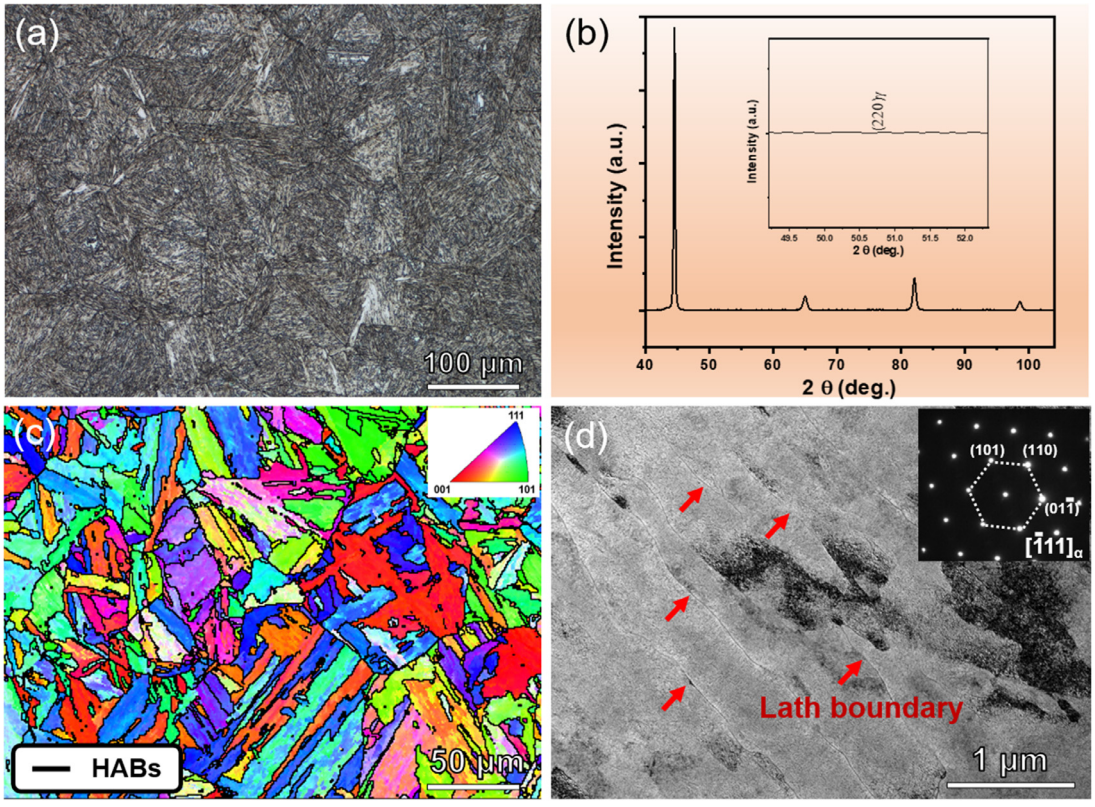

Fig. 4. Microstructures of sample A, (a) optical metallography image, (b) XRD pattern, (c) IPF map with HABs and (d) BF-TEM image with corresponding SAED pattern.

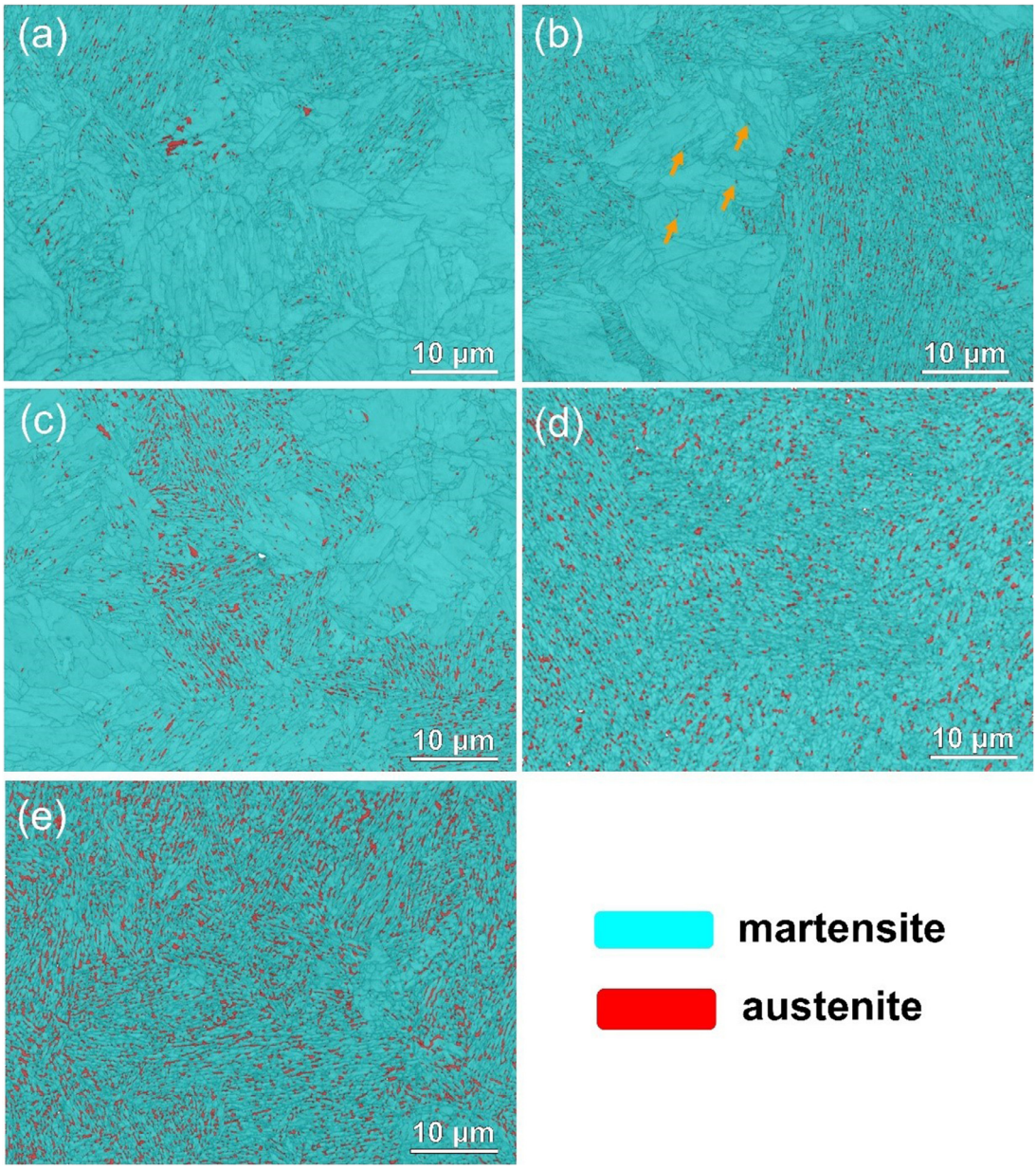

Fig. 5. BCE maps with the phases of samples with different numbers of CQT cycles from EBSD analysis: (a) sample B1, (b) sample B2, (c) sample B3, (d) sample B4, and (e) sample B6.

lyzed by TEM EDS point-scanning, which is shown in Table S2 in supplementary materials.

3.2.3.2. Ultrafine martensitic substructure. In Figs. 5 and 6, the morphology of these small austenite grains can be clearly distinguished. However, details of the martensitic microstructure could not be observed under these imaging conditions. Therefore, IPF maps with HABs were also constructed for samples with different numbers of CQT cycles. The IPF maps with HABs of samples B1–B4 are shown in Fig. 7(a–d), respectively. The substructure of martensite is gradually refined with increasing number of CQT cycles. In samples B1–B3, the martensite microstructure can be divided into refined regions and unrefined regions. The refined regions exhibit a type of ultrafine martensite substructure separated by HABs, while in the unrefined regions, the martensitic microstructure still presents as packets and blocks. When the number of CQT cycles is four (sample B4, Fig. 7(d)), the unrefined regions are all gone and the whole martensitic microstructure is dominated by the ultrafine martensitic substructure. The EGS of sample A and sample B1–B7 are shown in Fig. 7(e). The EGS abruptly drops from 5.57 (sample A) to 2 μm after a one-time cycle, and then decreases slowly but steadily to 0.5 μm.

The dimensions of martensitic laths are of the order of nanometers, so the TKD had to be employed in order to identify the changes in the martensite laths during CQT. The IPF map of sample A is shown in Fig. 8(a), where HABs shown by black lines and low-angle grain boundaries (LABs, misorientation angle less than 15° and greater than 2°) are decorated by white lines [27,28]. The width of the lath in sample A is around 500 nm, which is consistent with the TEM observation in Fig. 4(d). In sample B2 (Fig. 8(b)), the microstructure is divided into a refined region and an unrefined region, which is consistent with the results under EBSD in Fig. 7. In the unrefined regions, the crystallographic orientation of laths is still similar. In the case of four CQT cycles, the unrefined region disappears and is replaced by the refined region composed of various crystallographic orientations laths. Besides, it is interest-

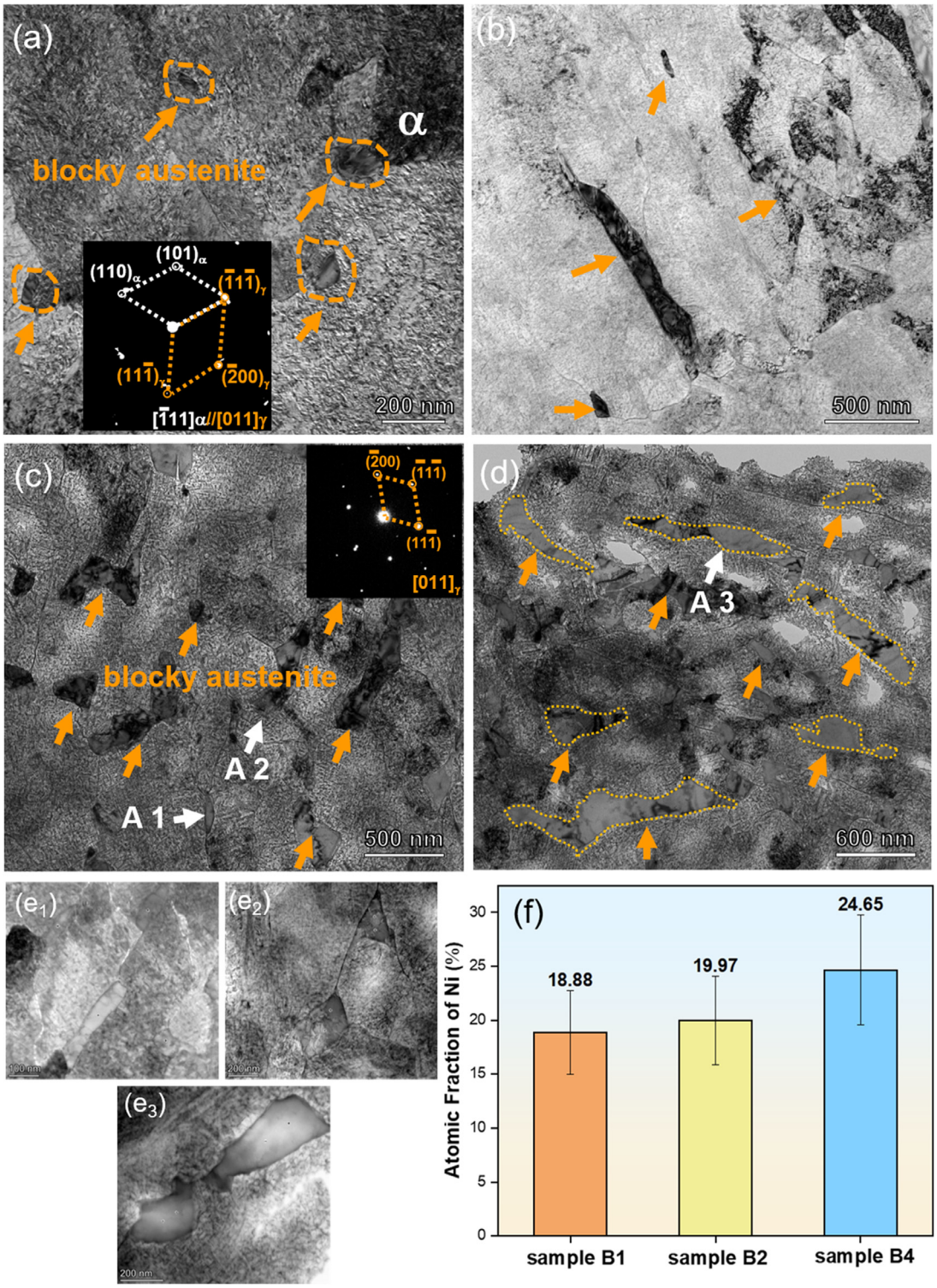

Fig. 6. BF-TEM images of (a) sample B1, (b) sample B2, (c) sample B4, and (d) sample B6; ABF-STEM images of (e_1) sample B1, (e_2) sample B2 and (e_3) sample B4; (f) EDS point-scanning analysis of Ni in austenite grains in (e_1–e_3).

ing that the lath boundaries which used to be thought of as LABs have been turned into HABs after CQT. The proportions of HABs and LABs in sample A are 12.9 % and 87.1 %, respectively. When the number of CQT cycles reaches 4 (sample B4), the proportion of HABs increases to 80.4 % while proportion of LABs decreases to 19.6 %. Although the LABs are of a high proportion in sample A, the percentage of HABs rises further with an increasing number of CQT cycles, as shown in Fig. 8(d).

The BC maps with austenite phase (red), HABs, and LABs in samples B2 and samples B4 are shown in Fig. 9(a, c), respectively, while the corresponding Ni element distribution is demonstrated in Fig. 9(b, d). In sample B2, the Ni content (wt.%) of austenite grains in the refined region is higher than that in the surroundings, while the Ni is homogeneously distributed in the unrefined region without austenite grains, as shown in Fig. 9(b), which is in agreement with the results in Fig. 6. Furthermore, it is worth

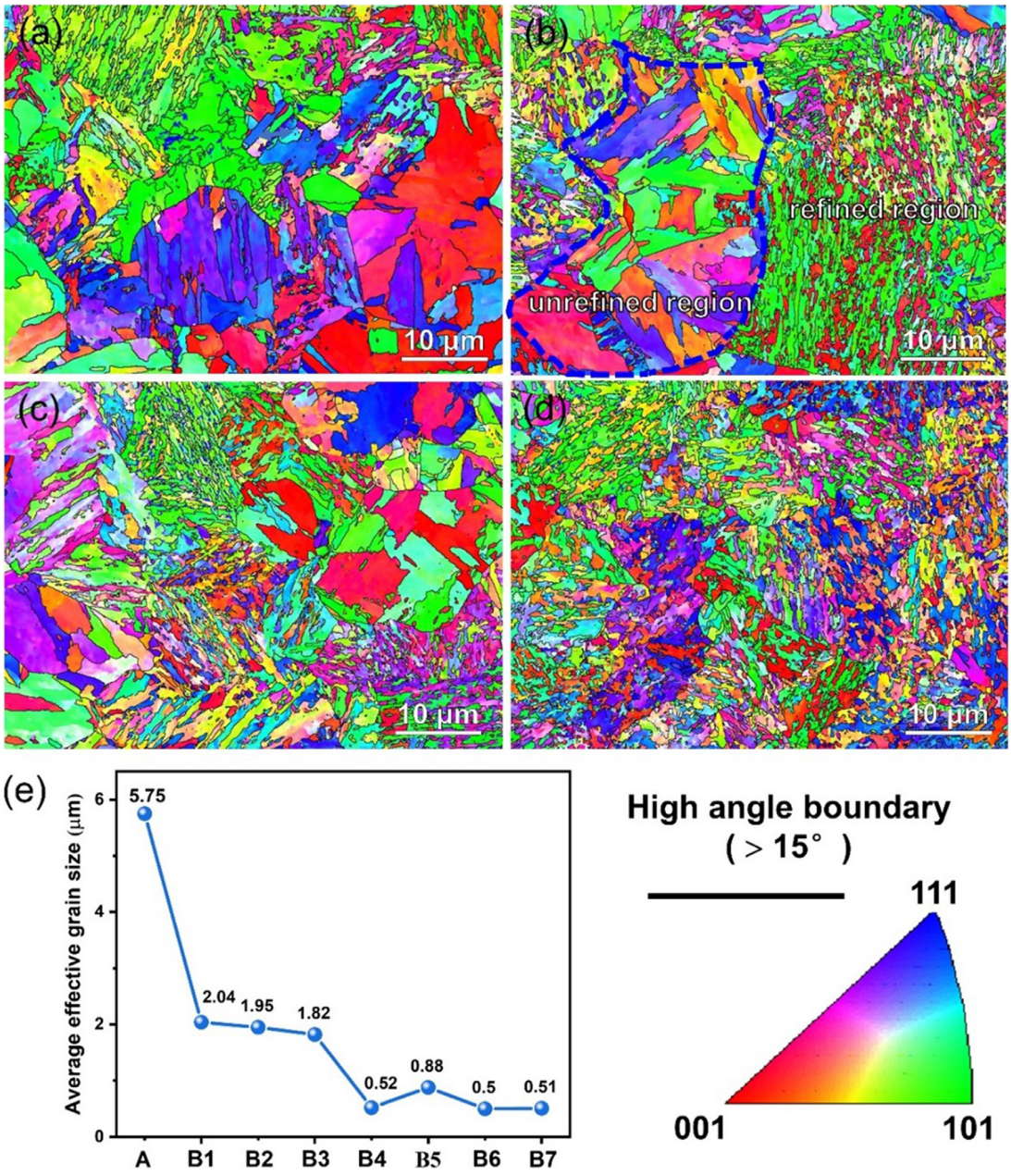

Fig. 7. IPF maps with HABs: (a) sample B1, (b) sample B2, (c) sample B3, (d) sample B4; (e) EGS of samples with different numbers of CQT cycles.

noticing that not only the Ni content in the small austenite grains is higher than in the martensitic matrix, but that the refined laths develop an inhomogeneous composition, as shown in Fig. 9(d). According to Ni element distribution characterization, the microstructure in sample B4 can be divided into three substructures: (i) Ni-rich austenite grains, (ii) Ni-rich martensite laths, and (iii) Ni-poor martensite laths. The Ni-rich austenite grains are identified to have an average Ni content of 24.6 % ± 0.8 %, higher than that of Ni-rich martensite, 23.2 % ± 0.2 %, demonstrating local Ni partitioning takes place during CQT, as seen in Fig. 9(e). Average content of all alloying elements in Ni-rich austenite grains, Ni-rich martensite laths of the sample B4 from TKD EDS point-scanning analysis are shown in Table S3 in supplementary materials.

The dilatation curves of samples with different numbers of CQT cycles measured during CQT also provide independent evidence that Ni partitioning occurs as shown in Fig. 9(f). Sample B1 has the lowest Ms temperature and exhibits a significant shrinkage of length during cooling. The magnitude of shrinkage decreases and Ms temperature rises with the increasing number of CQT cycles. Those regions with lower Ni content will undergo martensitic transformation at higher temperatures, while the regions with higher Ni content will undergo martensitic transformation at lower temperatures. This unusual change in martensite formation characteristics is clear evidence of the presence of Ni-poor and Ni-rich regions in the austenitic microstructure at the peak CQT temperature.

Given the potential influence of TKD technique resolution on experimental results, SAED analysis of the Ni-rich martensite region was conducted in TEM mode, as depicted in Fig. 10. The EDX-mapping (Fig. 10(b)) reveals that Ni element distribution is un-uniform within the microstructure. EDS line-scanning analysis (Fig. 10(c)) of the highlighted white circle region in Fig. 10(a) indicates elevated Ni content compared to its surrounding regions. To further characterize the crystal structure of the Ni-rich marten-

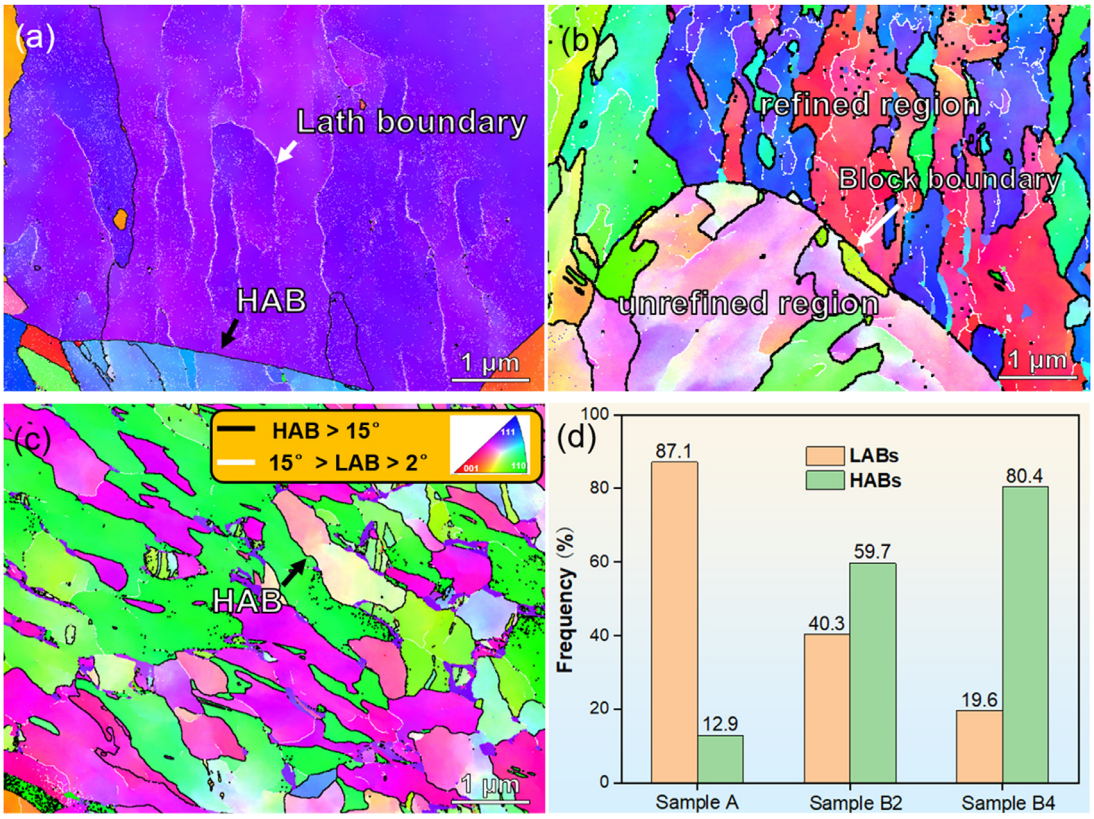

Fig. 8. IPF images with LABs (white lines) and HABs (black lines) from TKD analysis: (a) sample A, (b) sample B2, and (c) sample B4; (d) proportions of HABs and LABs in sample A, B2 and B4.

site, the SAED patterns of Ni-rich martensite lath along [100] and [$\bar{1}$11] zone axis were obtained, as shown in Fig. 10(d). It is assumed that the Ni-rich martensitic lath is BCT structure, implying that the interplanar spacings $a = b \neq c$ ($a > c$ or $a < c$) and the angles between the corresponding lattice planes are not equal to 60°. However, the angles between the corresponding lattice planes are measured to be 60°, indicating that the Ni-rich martensitic laths have BCC structure (Fig. 10(d_2)). In addition, the interplanar spacings of (010) and (001) lattice planes in Fig. 10(d_1) were measured to be approximately ~0.287 and ~0.284 nm, respectively, which were found to be quite equal and evidently consistent with the lattice parameter characteristics of the cubic crystal system. The SAED pattern obtained along the [$\bar{1}$11] was captured, and was measured to be approximately ~0.287 nm. Hereto, the Ni-rich martensite lath was totally verified to contain a BCC structure.

3.2.4. Precipitates after CQT

The details of the precipitates in samples B1, samples B2, samples B4, and samples B6 are presented in Fig. 11. A high number density of Ni_3Ti precipitates exists in the martensitic matrix in CQT samples. The results demonstrate that Ni local segregation during CQT does not affect the morphology and number density of precipitates. Besides, in sample B4, the orientation between the Ni_3Ti and martensite matrix follows $[011]_\alpha//[0001]_\eta$ relationship, as shown in Fig. 11(c) [3,29]. APT analysis of isosurfaces of 0.2 at.% Mo plus 0.35 at.% Ti concentration and proximity histograms in sample B4 shows that in addition to the rod-like Ni_3Ti, Mo-enriched precipitates also present in the matrix, as shown in Fig. 11(e). The lengths of the Ni_3Ti and the Mo-enriched precipitates are about 20 and 10 nm, respectively. The total number density of these two precipitates is $7.7 \times 10^{23}/m^3$.

To further substantiate that local Ni partitioning does not affect the precipitation behavior of the precipitates, the volume fractions of Ni_3Ti and Mo-enriched precipitates within the martensitic matrix were calculated using equilibrium phase diagrams for varying Ni contents of 14 %, 15 %, 16 %, and 18 % (wt.%), as depicted in Fig. S1. Remarkably, the volume fractions of Ni_3Ti and Mo-enriched precipitates remained consistent across different Ni concentrations.

4. Discussion

4.1. Formation of austenite grains and heterogeneous refined martensite laths

As to the formation of austenite grains and refinement and increased chemical heterogeneity of the martensite, the following aspects are worth noticing. At first, the Ni-rich austenite grains are introduced by CQT. Secondly, the austenite grains gradually grow as the number of CQT cycles increases and the Ni content in the austenite grains also increases, as shown in Fig. 6. Thirdly, in addition to the development of the Ni-rich austenite grains, the martensite laths are also refined during CQT. More interestingly, not only Ni-poor ultrafine laths are observed, but also Ni-rich ultrafine laths are seen, as shown in Fig. 9. From the above three aspects, it can be concluded that the formation of austenite grains and heterogeneous refined martensite laths are related to the local Ni partitioning during CQT. So, to further understand the relationship between Ni partitioning and the formation of these microstructures during CQT, the Thermo-Calc & DICTRA software in combination with the TCFE 8 and MOBFE 3 databases were applied to simulate the formation kinetics of austenite, local equilibrium of Ni at the austenite/martensite interface assuming a planar 1-D configuration, and elemental diffusion behavior in single phases [30,31]. The width of the simulation cell is acquired from Fig. 4 and the corresponding width of martensitic lath is set to 500 nm. An austenite nucleus with a width of 1 nm with a nominal composi-

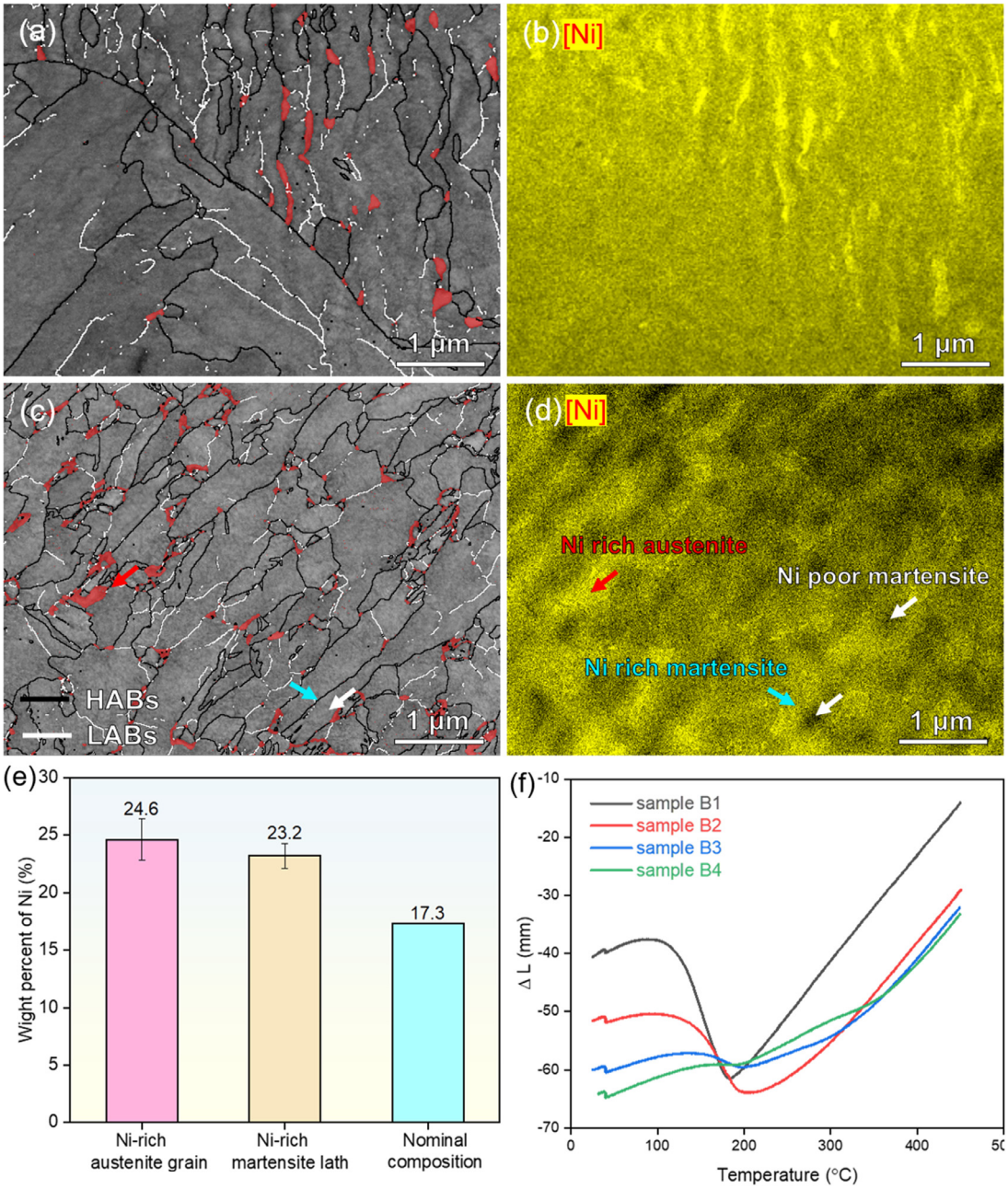

Fig. 9. BCE map with austenite phase (red), HABs, LABs, and corresponding Ni element distribution in (a, b) sample B2, (c, d) sample B4, (e) EDS point-scanning analysis of Ni-rich austenite grains and Ni-rich martensite laths, (f) dilatation of samples with different numbers of CQT cycles as a function of temperature.

tion is located at the right side of the martensitic region. The geometry principle of the nucleus for simulation has been explained in other studies [30–33]. The phase transformation kinetics and the phase boundary migration during the slow heating from 450 to 850 °C and subsequent holding for 15 min were simulated. To accurately account for the effect of heating rate and temperature on the formation mechanism of austenite, the same heating rate as the experimental process was adopted in the simulation [34]. During the phase transformation calculation, in the DICTRA simulations the austenite/martensite phase interface is assumed to maintain the local equilibrium state.

As the temperature rises, the kinetics of austenite formation in sample B1 can be divided into three stages, as shown in Fig. 12(a). When the temperature is lower than 550 °C, the fraction of austenite remains constant given that the temperature is relatively lower. For temperature range of 550 and 700 °C, the kinetic of austenite formation is accelerated gradually. When the temperature exceeds 700 °C, complete austenitization is progressively achieved. The final critical temperature in simulation results appears to be lower than that obtained by dilatometry (Fig. 1(a)), as the simulation does not take into account the nucleation process and solute drag effects [35–38]. The kinetics of austenite formation indicate that the austenite grains are formed during slow heating (between 550 and 700 °C). This conclusion is also supported by the results obtained from dilatometric experiments, as shown in Fig. 12(b). Figure 12(b) shows the dilatation as a function of time at 550, 600, and 650 °C for 3 h of holding. It was found that all samples show significant shrinkage, indicating austenitic grains forming during holding. In addition, the samples began to shrink at the initial stage of holding, indicating that austenite grains had already formed at this time. In the temperature range from 550 to 700 °C, the kinetics of austenite formation exhibit an increasing and

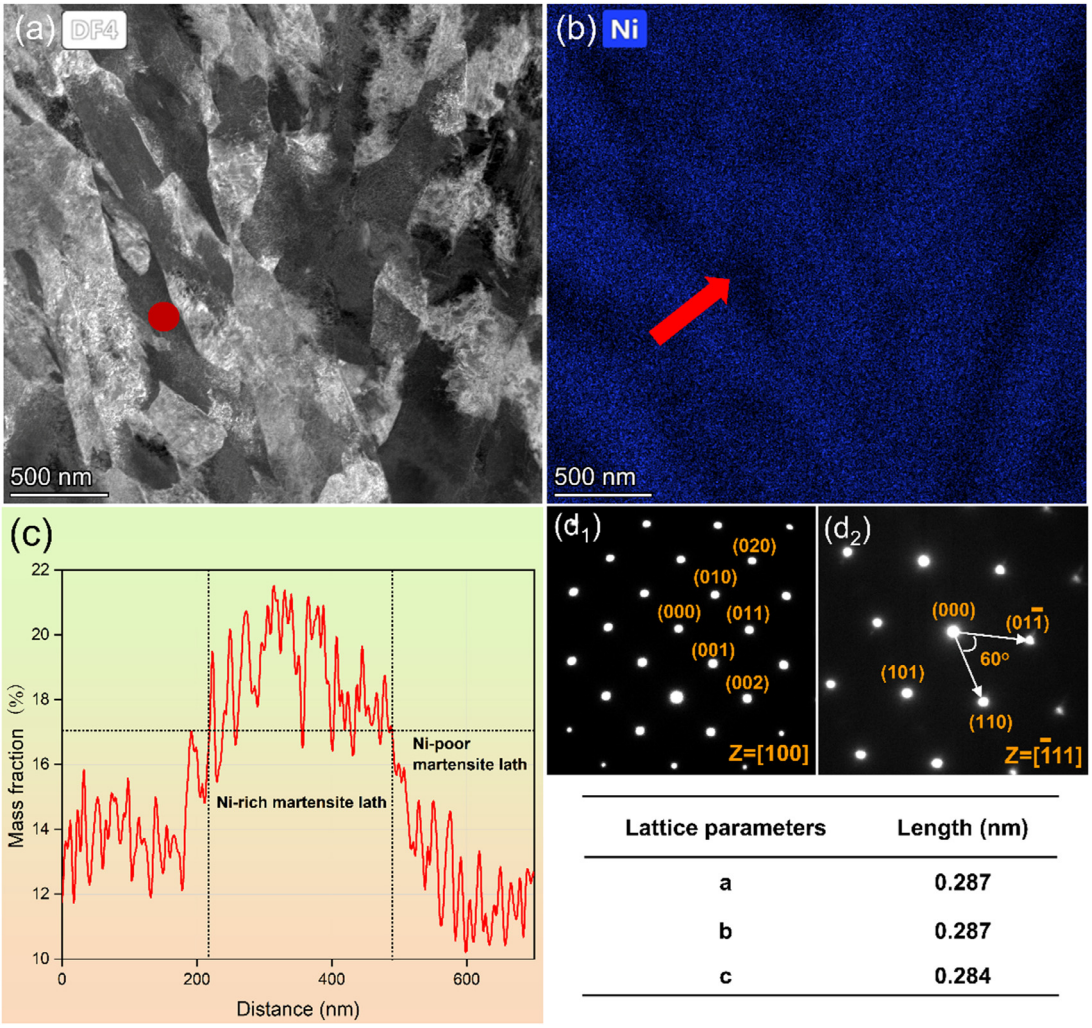

Lattice parameters	Length (nm)
a	0.287
b	0.287
c	0.284

Fig. 10. (a) BF-TEM image of sample B4, (b) corresponding Ni element distribution map, (c) line-scanning analysis of Ni in local region, (d) corresponding to SAED analysis of the region highlighted red circle region in Fig. 10(a).

subsequently decreasing trend, which is related to the Ni diffusion on both sides of the austenite and martensite. In the temperature range of 550–675 °C, Ni-poor peaks appear on the martensite side and Ni-rich peaks appear on the austenite side (Fig. 12(c)), implying that the Ni continuously diffuses from the martensite side towards the austenite side. According to thermodynamics, diffusion is driven by chemical potential which is a function of elemental concentration and temperature, and diffusion always takes place in the direction of decreasing chemical potential. Figure 12(d) shows the chemical potential as a function of Ni concentration at different temperatures, where the Ni concentration in different regions in the simulation cell at different temperatures is given by Fig. 12(c). It can be seen that the Ni chemical potential of the austenite side is lower than that of the martensite side, indicating that the diffusion of Ni into the austenite leads to a progressive increase of the Ni concentration in the austenite and the formation of Ni-poor regions on the martensite side. Besides, the phase transformation in this temperature interval follows a partitioned local equilibrium (PLE) model, where the slow diffusion of Ni in the martensite controls the growth of austenite [32]. As the temperature increases, the kinetics of austenite formation reaches the maximum value at 675 °C. From the distribution of Ni at this moment, it can be seen that the width of the Ni-poor peak in martensite gradually becomes narrower, implying that the diffusion of Ni in the martensite is no longer a controlling factor for phase transformation. The phase interface approaches the Negligible-partitioning local equilibrium (NPLE) mode at this temperature [39,40]. As the temperature exceeds 675 °C, the kinetics of austenite formation slows down. At this moment, the width of Ni depleted peak in martensite gradually becomes broader again, indicating that the long-distance diffusion of Ni occurs again within the martensite region. The diffusion of Ni in martensite gradually becomes the main factor controlling the phase transformation again. As the temperature rises, the microstructure approaches the single-phase of austenite according to the equilibrium phase diagram.

When the temperature reached 850 °C, full austenitization has been achieved, i.e., the microstructure is single-phase austenite. This is evidenced by the fact that the dilatation rate of samples B1–B4 remains unchanged when held at 850 °C for 15 min, as shown in Fig. 13(a). However, there is still a large Ni concentration gradient in the single-phase austenite. The Ni concentration at different regions in the simulation cell as a function of holding time is shown in Fig. 13(b) and the chemical potential of Ni in different regions for different holding times in the single-phase austenite is shown in Fig. 13(c). It can be seen that the Ni chemical potential in the high Ni concentration region is higher than that in the lower Ni concentration region, indicating that Ni diffuses from the Ni-rich region to the Ni-poor region. In other words, the Ni in the Ni-rich austenite formed during the slow heating diffuses to the region with a lower Ni concentration, resulting in

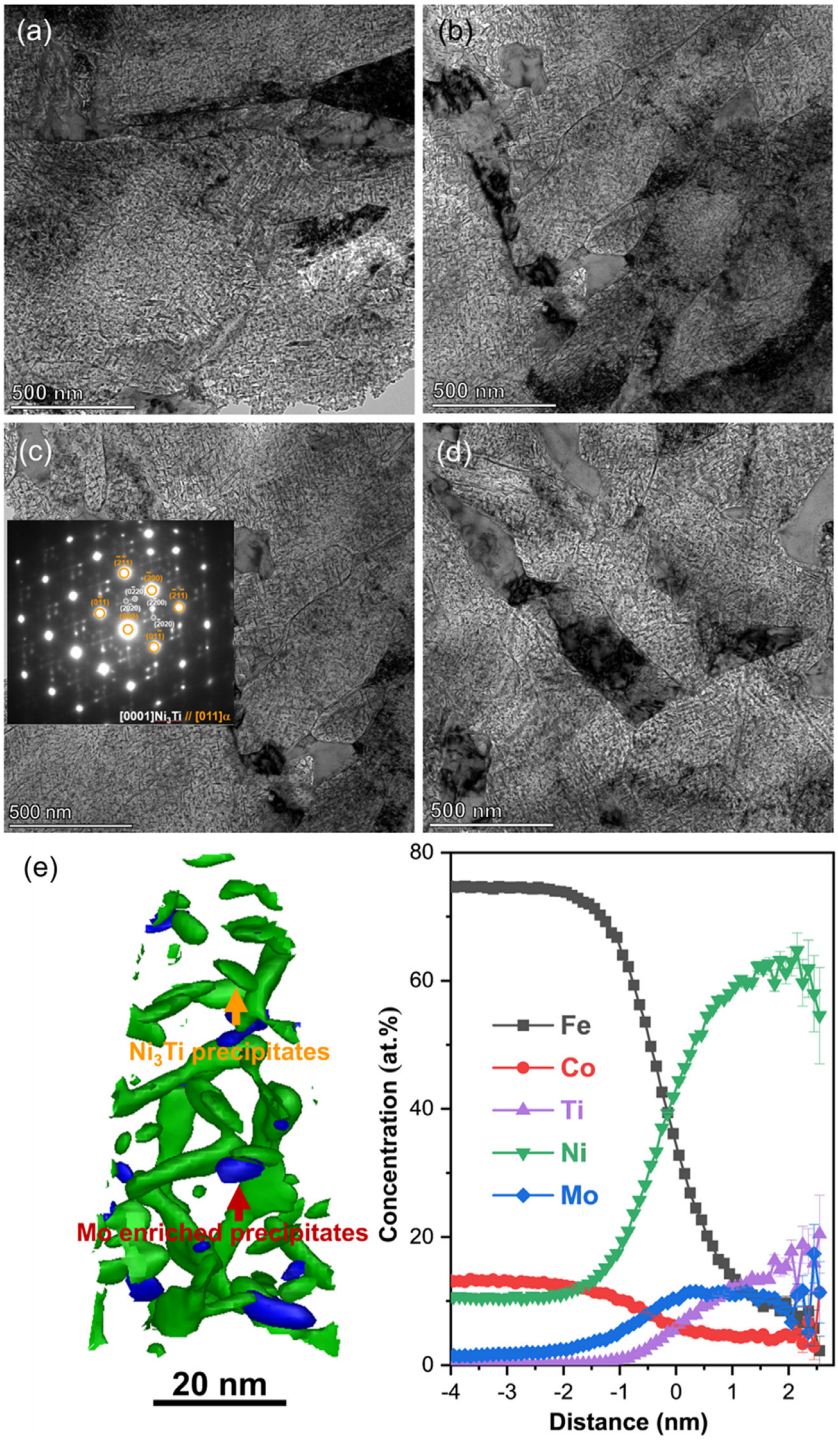

Fig. 11. (a) BF-TEM images of precipitates in (a) sample B1, (b) sample B2, (c) sample B4, (d) sample B6, (e) isosurfaces of 0.2 at.% Mo plus 0.35 at.% Ti concentration and proximity histograms of Ni_3Ti and Mo enriched phase from APT analysis in sample B4.

a decrease of Ni concentration in some of the Ni-rich austenite grains.

However, even though the chemical heterogeneity is reduced after holding treatment at 850 °C for 15 min, the distribution of Ni in the simulation cell at the austenitization stage is still not uniform, as shown in Fig. 13(d) (red line). The Ms temperature at each grid point was calculated according to Ref. [41] based on the alloy composition of the computational domain at the end of the holding treatment. The calculation results show that 3 % (vol.) of the austenite has a Ms temperature below RT (blue line), indicating that these austenite grains can be retained after cooling. Meanwhile, the rest of the austenite is transformed into two types of martensite, namely Ni-rich and Ni-poor, unlike the case of sample A in which a chemically homogeneous austenite is formed resulting in a sharp and well-defined martensite formation.

Some small austenitic grains were indeed observed between the martensitic laths in sample B1 (Fig. 6(a)). In addition, heterogeneity of Ni is already present in some regions of sample B1. These factors may have an impact on the subsequent kinetics of austen-

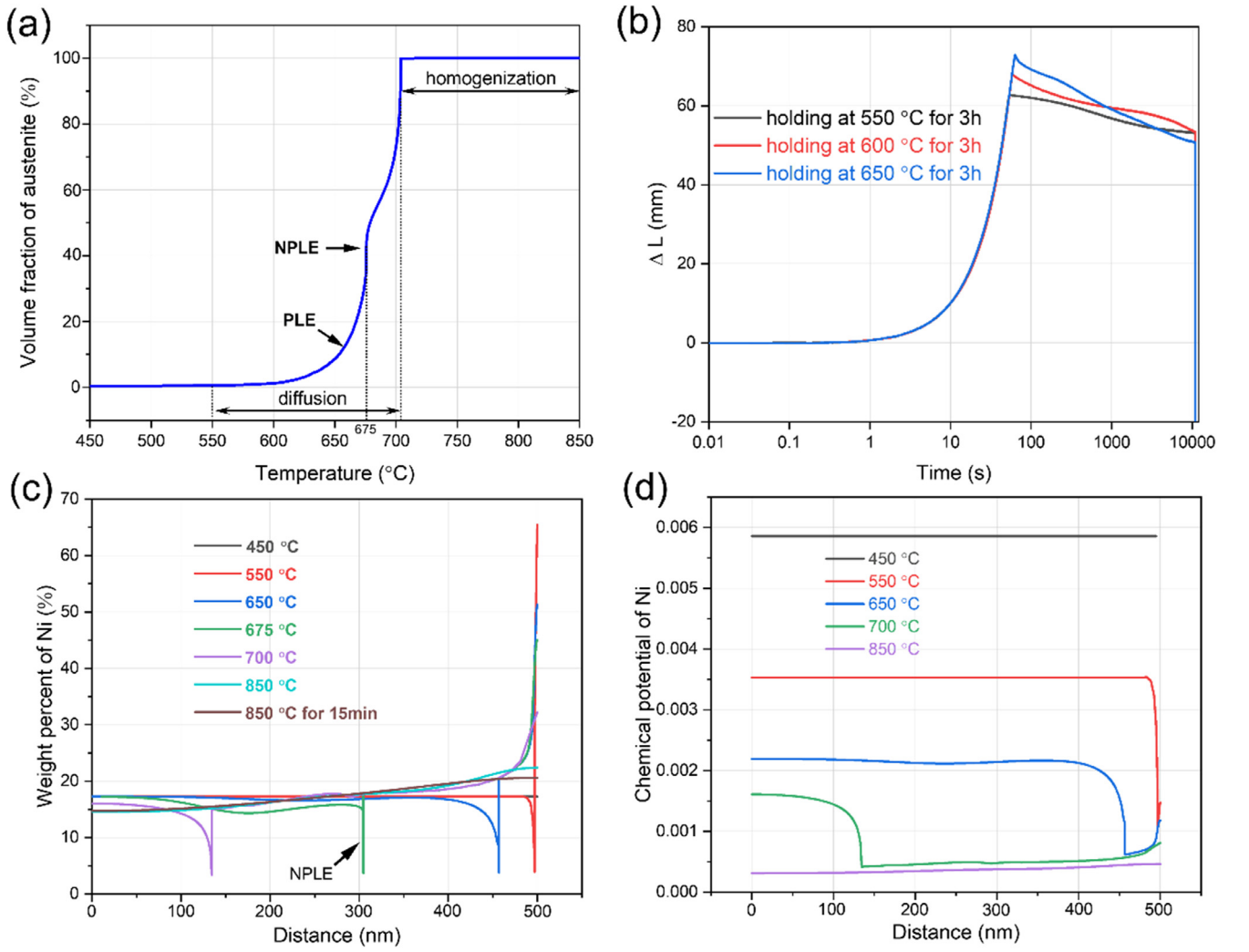

Fig. 12. (a) Kinetics of austenite formation in the sample B1 during the CQT, (b) dilatation as a function of time at 550, 600 and 650 °C for 3 h, (c) Ni weight percent at different temperatures in different regions of the simulation cell, (d) Ni chemical potential at different temperatures in different regions of the simulation cell.

ite formation in sample B2. Therefore, the simulation cell for the second cycle of CQT was not full martensite, but rather there were austenite grains with a fraction of 3 % (vol.) in a chemical heterogeneous martensitic matrix.

In the DICTRA simulation of the second cycle of CQT, the width of martensite was set to 485 nm, with an additional 15 nm of austenite to its right, as shown in Fig. 14(a). In addition, the composition profile in the matrix obtained from the last stage of the sample B1 simulation was introduced into the computational domain of sample B2. The kinetics of austenite formation in the second cycle of CQT is similar to that of the first cycle of CQT. The formation rate of austenite increases with temperature, reaches a maximum at 674 °C, and then decreases, achieving complete austenitization at about 700 °C, as shown in Fig. 14(b). From the distribution of Ni at different temperatures in Fig. 14(c), it can be seen that when the temperature is lower than 650 °C, the formation of austenite is relatively slow, and there is a broader Ni-poor peak in martensite. As the temperature increases, the phase transformation kinetic is accelerated and the Ni-poor peaks in martensite gradually become narrower. When the temperature is further increased, the Ni-poor peaks in martensite become wider again, indicating that the phase transformation rate slows down. The evolution of Ni-poor peaks within the martensite indicates that Ni continues to diffuse into the austenite side during heating. This leads to a further increase in the Ni concentration in the Ni-rich austenite and the formation of a Ni-poor region on the martensite side. At the austenitizing stage, Ni is still diffusing from the Ni-rich region to the Ni-poor region. Nevertheless, comparing the composition profiles in sample B1 and sample B2 at the end of the holding, it can be seen that the Ni concentration in the Ni-rich region of sample B2 is higher than that of sample B1, while the Ni-poor region is lower than that of sample B1. The simulation results suggest the Ni heterogeneity in microstructure intensifies progressively with the increasing number of CQT cycles, which is consistent with the dilatation results (Fig. 9(g)). The Ms temperature at each grid point was calculated based on the alloy composition of the computational domain after holding at 850 °C for 15 min, as shown in Fig. 14(d). The calculation results show that austenite with a width of 76 nm has a Ms temperature below RT, which indicates that those austenite grains will be retained, while the rest of the austenite will be transformed into Ni-rich and Ni-poor martensite after water cooling. It can be seen that local Ni partitioning leads to the formation of small Ni-rich austenite grains, Ni-rich martensite laths, and Ni-poor martensite laths. After the four CQT cycles, the Ni content in Ni-rich austenite grains and Ni-rich martensite rises to 23.48 % and 22.1 %, respectively. The above analysis reveals that each CQT cycle increases the Ni content variance and promotes Ni heterogeneity.

It is essential to emphasize the significance of a slow heating rate for Ni partitioning. Lee et al. [42] conducted a study inves-

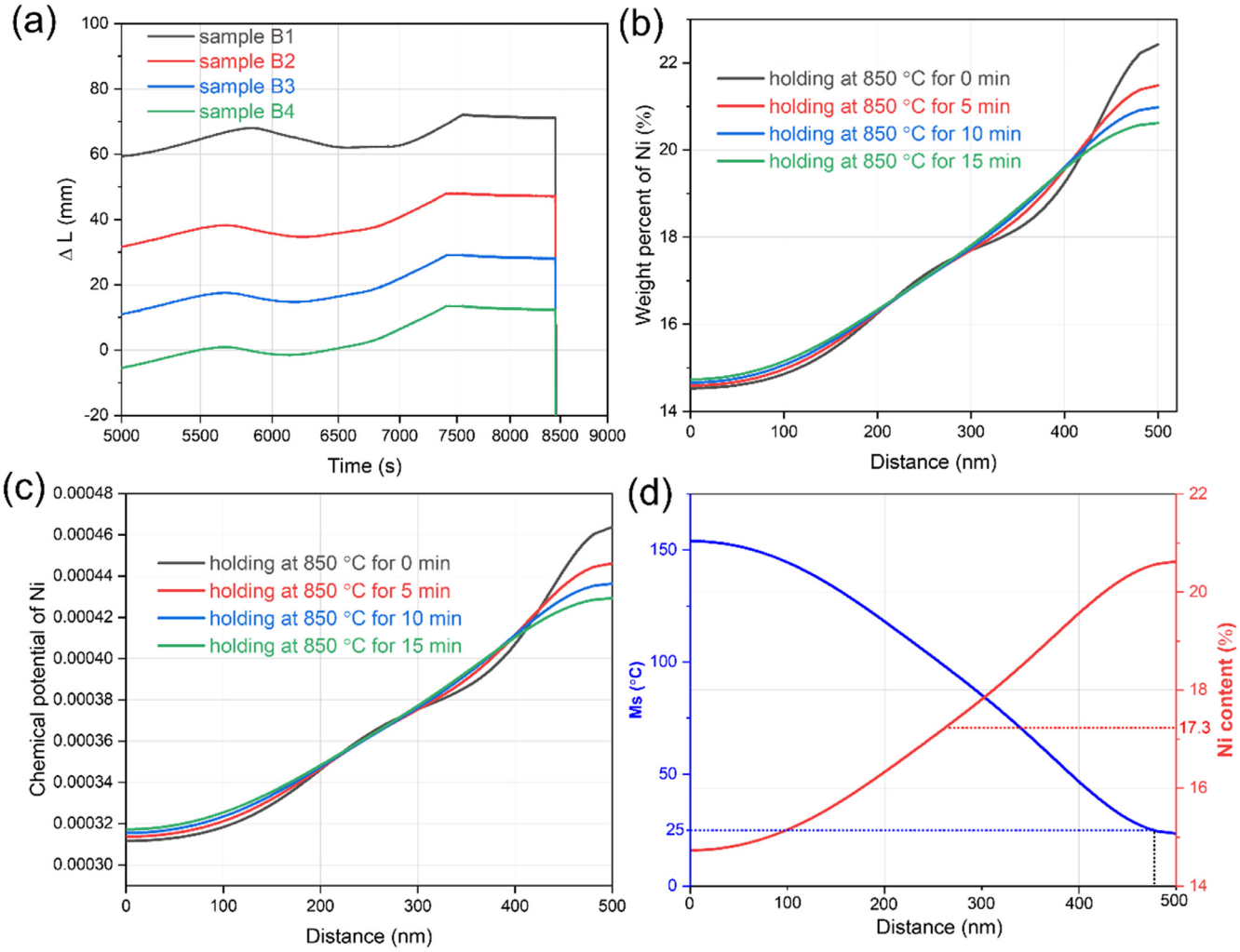

Fig. 13. (a) Dilatation as a function of time of sample B1–B4, (b) Ni weight percent as a function of holding time at 850 °C, (c) Ni chemical potential in the simulation cell at different regions for different holding times, (d) Ni content and Ms temperature at each grid point calculated from the Ni content at the end of the holding in the simulation cell.

tigating the impact of heating rate on the martensite-to-austenite transformation in martensitic stainless steels. They discovered that when the heating rate was less than 10 K/s, the austenite reversion was governed by a diffusion mechanism, whereas it shifted to a shear mechanism without diffusion when the heating rate exceeded 10 K/s. In order to further corroborate that this microstructure forms during slow heating in CQT, additional CQT experiments with rapid heating were conducted, employing a heating rate of approximately 50 °C/s and the samples were labeled as sample C1–C4 according to the number of CQT cycles. Figure S2(a, b) shows the IPF map with HABs and the phase distribution in BC mode of sample C4, respectively. The sample C4 exhibited a martensitic microstructure that remained unrefined, with no austenite grains detected. Furthermore, the dilatation curves of samples C1–C4 showed no significant change in the Ms temperature, indicating that rapid heating rates do not lead to Ni elemental partitioning.

Moreover, only blocky austenite grains were observed, with no presence of film-like austenite grains in the samples with the number of CQT cycles. This is due to the fact that all film-like austenite grains develop into blocky austenite as the temperature increases during single cycle. To validate this, the experimental steels were aged at 550 and 600 °C for 3 h, respectively. BF-TEM images revealed the presence of film-like austenite grains with an average width of 20 nm after aging at 550 °C for 3 h (Fig. S3(a)), whereas aging at 600 °C for 3 h resulted in the observation of only blocky austenite grains with an average width of 500 nm (Fig. S3(b)).

4.2. Development of mechanical properties with the cycle numbers of CQT

4.2.1. Effect of CQT on strength

The plot illustrating mechanical properties (Fig. 2(a)) versus the number of CQT cycles indicates that with fewer than 4 cycles, both UTS and YS remain unaltered. However, when the cycle number exceeds 4, as evidenced by samples B5–B7, a slight decrease in UTS is observed, accompanied by a significant reduction in YS. This change in strength is intricately linked to the microstructural evolution during CQT. Figs. 5 and 6 reveal a gradual increase in the volume fraction and size of austenite grains with increasing in cycle number of CQT. In sample B4, the microstructure contains blocky austenite grains with a width of 500 nm and a volume fraction of 6.59%. Surprisingly, the strength remains at 2.3 GPa, contrary to the general finding that a higher fraction of blocky austenite grains often reduces the strength of ultra-high-strength steels (UHSS). The absence of a reduction in UTS can potentially be attributed to three factors. Firstly, the matrix is strengthened by the Ni_3Ti and Mo-enriched precipitates. Despite significant local Ni segregation during CQT, the precipitation behavior of precipitates remains unaffected, as shown in Figs. 11 and 12. These high-

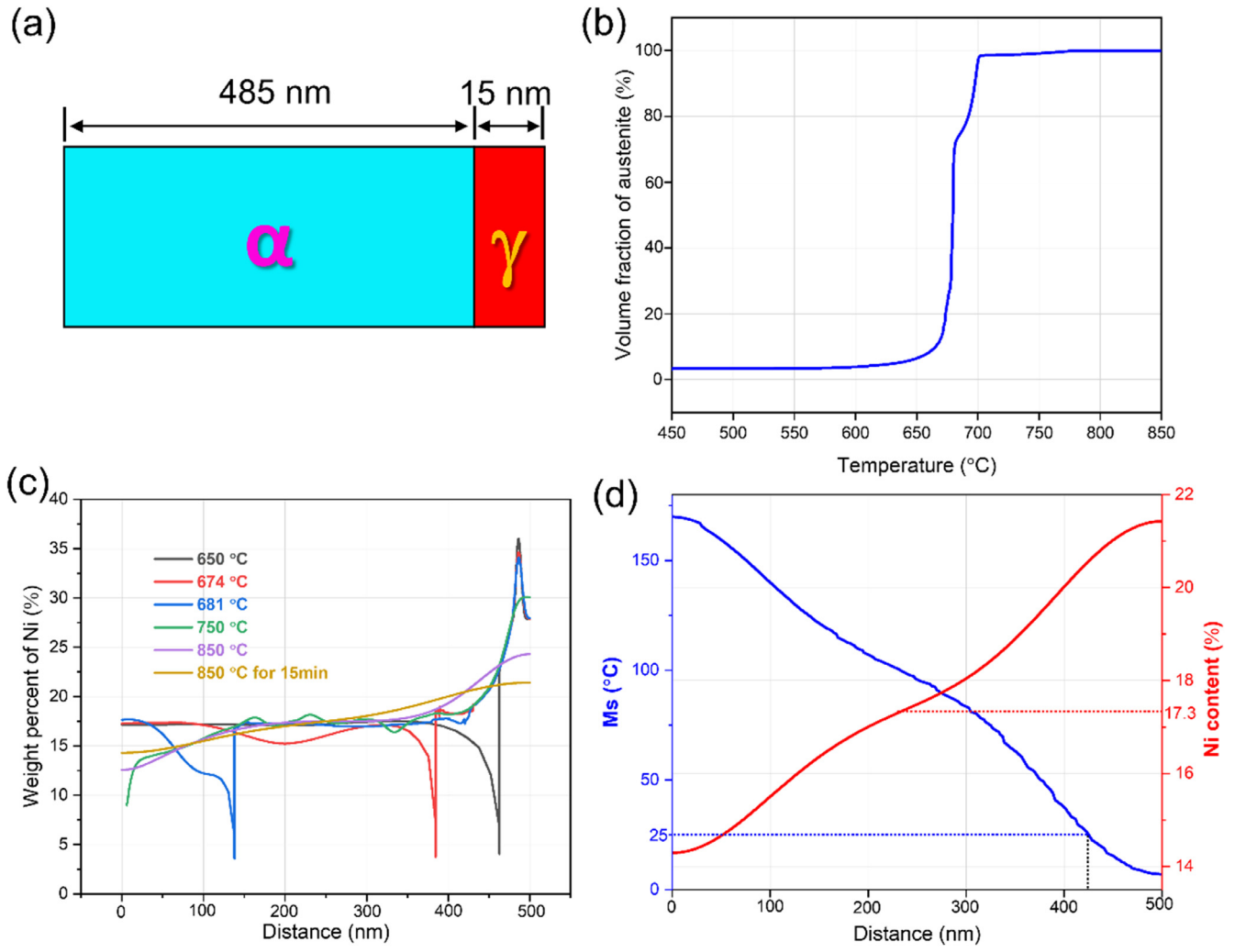

Fig. 14. DICTRA simulation results of the sample subjected to the second cycle of CQT, (a) simulation cell, (b) kinetics of austenite formation as the function of temperature, (c) Ni weight percent at different temperatures in different regions of the simulation cell, (d) Ni content and Ms temperature at each grid point calculated from the Ni content at the end of the holding in the simulation cell.

density nanoscale precipitates act as barriers to reduce dislocation movement, thereby enhancing the strength of CQT samples [43,44]. For samples B1–B4, no precipitates were observed in the austenite grains themselves. Secondly, the refinement of laths contributes to strengthening. The initial lath boundaries have gradually shifted from LABs to HABs during CQT, significantly increasing the proportion of HABs (Fig. 8(d)), although the size of the PAG did not decrease due to CQT (Fig. 3). Several studies have shown that the UTS can be increased by increasing the proportion of HABs since dislocations have difficulty passing through HABs, but the resistance to crossing LABs is almost nonexistent [45]. Another factor playing a role in the retention of the strength with the number of CQT is the presence of sharp local fluctuations in Ni (and Mo levels) present just before the quenching step, the so-called Chemical Boundary Engineering concept presented by Ding et al. [46], who showed that in medium manganese automotive steels local portioning of Mn due to tailored cyclic treatments may lead to martensite reinforcement as the Mn-rich regions lead to obstacles in martensite formation and an exceptional combination of strength and ductility. Likely, the Ni partitioning in the CQT treatment in this maraging steel works in a similar way.

Although the volume fraction of blocky austenite grains in sample B4 reaches nearly 7 %, it exerts minimal impact on strength. This is attributed to higher hardness martensite surrounding the austenite grains, which can shield the austenite from externally applied loads, known as the “shielding effect”. However, the YS of the experimental steel decreases significantly once the cycle number of CQT exceeds 5. Despite exhibiting similar characteristics in terms of PAG size, EGS, and the number density of precipitates, sample B6 differs from sample B4 in terms of higher volume fraction and size of austenite grains. Therefore, the YS reduction observed in samples B5–B7 may be attributed to the enlargement of austenite grain size, rendering the high-strength martensite incapable of effectively shielding these larger austenite grains. Under stress, the larger-sized austenite grains tend to yield preferentially to the martensitic matrix. Although some austenite grains may transform into martensite under stress, thereby enhancing strength to some extent, the strength of fresh martensite remains considerably lower than that of the martensitic matrix strengthened by precipitates. Consequently, the YS of the samples decreases. However, the UTS of samples B5–B7 appears relatively unaffected, owing to the TRIP effect occurring within the larger austenite grains during the tensile process, thereby augmenting their tensile strength.

4.2.2. *Effect of CQT on toughness*

The impact toughness of the experimental steel increases with the refinement of the martensitic laths and the increase in the

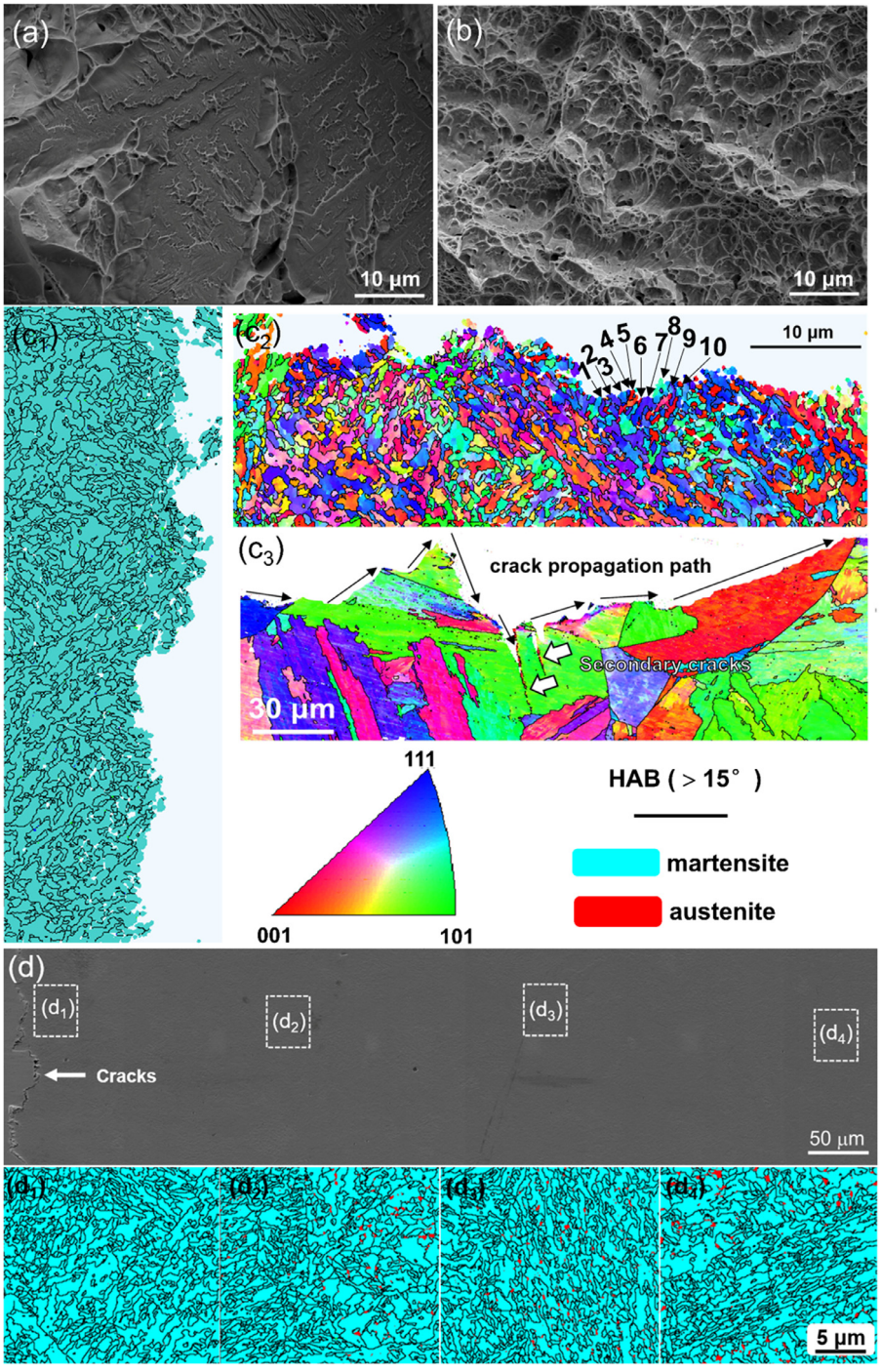

Fig. 15. Fractography after Charpy V-notch impact test: (a) sample A, (b) sample B4; (c_1) phase map and (c_2) IPF maps with HABs near the fracture of sample B4; (c_3) IPF maps with HABs near the fracture of sample A, (d) EBSD images near fracture of sample B4, the phase maps with HABs at position d_1–d_4.

austenite grains volume fraction during CQT. SEM analysis of the fracture of sample A and sample B4 showed that the fracture of sample A was a cleavage fracture, as shown in Fig. 15(a), while the fracture of sample B4 was characterized by ductile dimpled fractures, which consisted of fine equiaxed dimples and micro-voids, as shown in Fig. 15(b). The phase map and IPF map with HABs near the fracture of sample B4 are shown in Fig. 15(c_1, c_2), respectively, and the misorientation angles between adjacent zones are listed in Table S4 in supplementary materials. The zone surrounded by crystallographic misorientations of less than 15° represents a unit. It can be seen from Table S4 that crystallographic misorientation between adjacent zones is large and greater than 15° (boundaries are HABs). From Fig. 15(c_2), it can be seen that when the cleavage crack encounters zone 7, it is arrested and then deflected by a larger angle. Therefore, more energy is needed for the cleavage crack [43,44]. When the cracks are produced in sample A, the cracks will propagate along the straight HABs, and the cracks will expand very fast without much resistance, as shown in Fig. 15(c_3). In contrast, in sample B4, the cracks also propagate along HABs, but its propagation path becomes long and tortuous, which consumes more energy. The interaction between multi-phase and crack propagation is a key fac-

tor in improving toughness. The misorientation angles between austenite grains and ultra-fined martensite laths are very different, resulting in cracks deflecting. Besides, the compressive stress caused by the volumetric expansion of the austenite-to-martensite transformation can blunt the crack tip and further resist crack propagation.

The formation of austenite grains is another reason for the increase in toughness. Austenite grains, serving as soft phases, effectively blunt the crack tip and trigger a martensitic transformation under stress, known as the TRIP effect [47–49], thereby absorbing energy. A related study [50] demonstrated that austenitic grains can delay the nucleation of micropores by alleviating tension on their nucleated surfaces, or they can counteract the strain softening effect induced by micropore nucleation through the hardening effect induced by their phase transformation. Additionally, austenite exhibits lower strength compared to martensite and is more prone to plastic deformation, thus enhancing stress distribution. Austenite grains, i.e., un-transformed grains, are not found near the fracture surface of broken sample B4, but a small quantity of austenite is found at a distance from the fracture surface, as shown in Fig. 15(d_1–d_4), which confirms that stress-induced martensitic transformation has occurred locally in the vicinity of the crack path. Although these austenite grains are small and have a high Ni content, which improves the mechanical stability of the austenite to some extent, the localized plastic deformation produced during the impact test transforms the austenite to martensite, which will result in the absorption of additional energy and thus the impact toughness is improved.

5. Conclusions

In the present research, the cyclic quenching treatment (CQT) has successfully improved the RT Charpy V-notch impact energy of experimental maraging steel from 9 to 20 J, while keeping the tensile strength at a high level of 2.3 GPa. The following conclusions have been drawn:

1) The improvement in mechanical properties and impact toughness due to CQT in the present research is not due to a progressive refinement of the prior austenite grain size.
2) With an increasing number of CQT cycles, the martensitic microstructure has been remarkably refined due to the formation of Ni-rich austenite grains, Ni-rich laths, and Ni-poor laths. When the CQT is applied less than 4 times, unrefined block regions could still be seen. However, as long as the austenite grains are present, the microstructure is refined.
3) The boundaries between the Ni-rich austenite grains and two types of martensite laths are HABs, while boundaries between Ni-rich laths and Ni-poor laths can be either HABs or LABs.
4) The improved RT Charpy V-notch impact energy without loss of strength is owing to the refined substructure and the TRIP effect of austenite grains.
5) Local Ni segregation during CQT is responsible for the formation of austenite grains, Ni-rich martensite, and Ni-poor martensite, which could be well interpreted by the DICTRA simulation. However, it is still unknown why the refinement of microstructure in different regions is not synchronous.

Declaration of competing interest

The authors declare that they have no known competing financial interests or personal relationships that could have appeared to influence the work reported in this paper.

Acknowledgments

This work was sponsored by the National Natural Science Foundation of China (Grant Nos. 52271122, 52203384).

Supplementary materials

Supplementary material associated with this article can be found, in the online version, at doi:10.1016/j.jmst.2024.05.026.

References

[1] J. Green, J. Quest, Prog. Aeronaut. Sci. 47 (2011) 319–368.
[2] Y. He, K. Yang, K. Liu, W. Sha, Z. Guo, Metall. Mater. Trans. A 37 (2006) 1107–1116.
[3] V.K. Vasudevan, S.J. Kim, C.M. Wayman, Metall. Trans. A 24A (1990) 2655–2668.
[4] L.J. Wang, S.H. Jiang, B. Peng, B.H. Bai, X.C. Liu, C.R. Li, X.J. Liu, X.Y. Yuan, H.H. Zhu, Y. Wu, H. Wang, X.B. Zhang, Z.P. Lu, J. Mater. Sci. Technol. 161 (2023) 245–257.
[5] T. Liu, Z. Cao, H. Wang, G. Wu, J. Jin, W. Cao, Scr. Mater. 178 (2020) 285–289.
[6] Z.B. Jiao, J.H. Luan, M.K. Miller, Y.W. Chung, C.T. Liu, Mater. Today 20 (2017) 142–154.
[7] Y.K. Kim, K.S. Kim, Y.B. Song, J.H. Park, K.A. Lee, J. Mater. Sci. Technol. 66 (2021) 36–45.
[8] D.T. Han, Y.B. Xu, F. Peng, Y. Zou, R.D.K. Misra, J. Mater. Sci. 55 (2019) 4437–4452.
[9] H. Godin, J.D. Mithieux, C. Parrens, G. Badinier, M. Sennour, A.F. Gourgues-Lorenzon, Mater. Sci. Eng. A 742 (2019) 597–607.
[10] M. Vollmer, S. Degener, A. Bolender, A. Bauer, A. Liehr, A. Stark, N. Schell, P. Barriobero-Vila, G. Requena, T. Niendorf, Acta Mater. 257 (2023) 119168.
[11] B.B. Wu, X.L. Wang, Z.Q. Wang, J.X. Zhao, Y.H. Jin, C.S. Wang, C.J. Shang, R.D.K. Misra, Mater. Sci. Eng. A 745 (2019) 126–136.
[12] E. El-Shenawy, R. Reda, J. Mater. Res. Technol. 8 (2019) 2819–2831.
[13] G. Mandal, S.K. Ghosh, S. Chatterjee, Mater. Today-Proc. 18 (2019) 5196–5201.
[14] H. Luo, X. Wang, Z. Liu, Z. Yang, J. Mater. Sci. Technol. 51 (2020) 130–136.
[15] F.F. Conde, J.D. Escobar, J.P. Oliveira, M. Béreš, A.L. Jardini, W.W. Bose, J.A. Avila, Mater. Sci. Eng. A 758 (2019) 192–201.
[16] K. Nakazawa, Y. Kawabe, S. Mlineki, Mater. Sci. Eng. 33 (1978) 49–56.
[17] A. Saha, D.K. Mondal, J. Maity, Mater. Sci. Eng. A 527 (2010) 4001–4007.
[18] B. Smoljan, J. Mater. Proc. Technol. 155–156 (2004) 1704–1707.
[19] H. Hou, H.F. Li, Y.C. Jin, X.R. Wang, Z.Q. Wen, Mater. Sci. Eng. A 601 (2014) 1–6.
[20] N. Isasti, D. Jorge-Badiola, M.L. Taheri, P. Uranga, Metall. Mater. Trans. A 44 (2013) 3552–3563.
[21] H.T. Zhao, E.J. Palmiere, Mater. Charact. 158 (2019) 109990.
[22] J.H. Yan, P. Xue, L.Q. Zhang, L. You, X.D. Zhu, X. Wei, Mater. Sci. Eng. A 888 (2023) 145794.
[23] T. Tokarski, G. Nolze, A. Winkelmann, Ł. Rychłowski, P. Bała, G. Cios, Ultramicroscopy 230 (2021) 113372.
[24] C. Zhang, C. Wang, S.L. Zhang, Y.L. Ding, Q.L. Ge, J. Su, Mater. Sci. Eng. A 806 (2021) 140763.
[25] C. Kuehmann, B. Tufts, P. Trester, Adv. Mater. Processes 166 (2008) 37–40.
[26] T. Simson, J. Koch, J. Rosenthal, M. Kepka, M. Zetek, I. Zetková, G. Wolf, P. Tomčík, J. Kulhánek, Procedia Struct. Integr. 17 (2019) 843–849.
[27] S. Morito, H. Yoshida, T. Maki, X. Huang, Mater. Sci. Eng. A 438–440 (2006) 237–240.
[28] A.F. Gourgues, Mater. Sci. Technol. 18 (2013) 119–133.
[29] U.K. Viswanathan, G.K. Dey, M.K. Asundi, Metall. Trans. A 24A (1993) 2429–2442.
[30] X. Zhang, G. Miyamoto, T. Kaneshita, Y. Yoshida, Y. Toji, T. Furuhara, Acta Mater. 154 (2018) 1–13.
[31] X.G. Zhang, Y.J. Ren, J. Zhang, X.D. Yang, X. Xie, H. Liu, W.C. Yang, Mater. Charact. 190 (2022) 112025.
[32] R. Ding, Z. Dai, M. Huang, Z. Yang, C. Zhang, H. Chen, Acta Mater. 147 (2018) 59–69.
[33] C. Jia, C. Zheng, D. Li, J. Mater. Sci. Technol. 47 (2020) 1–9.
[34] Y. Zou, Y.B. Xu, G. Wang, Y. Han, H.X. Teng, D.T. Han, M.S. Qiu, F. Yang, R.D.K. Misra, Mater. Sci. Eng. A 802 (2021) 140636.
[35] O. Dmitrieva, D. Ponge, G. Inden, J. Millán, P. Choi, J. Sietsma, D. Raabe, Acta Mater. 59 (2011) 364–374.
[36] C. Qiu, H.S. Zurob, C.R. Hutchinson, Acta Mater. 100 (2015) 333–343.
[37] W.W. Sun, H.S. Zurob, C.R. Hutchinson, Acta Mater. 139 (2017) 62–74.
[38] E. Gamsjäger, Acta Mater. 55 (2007) 4823–4833.
[39] N. Nakada, K. Mizutani, T. Tsuchiyama, S. Takaki, Acta Mater. 65 (2014) 251–258.
[40] R. Wei, M. Enomoto, R. Hadian, H.S. Zurob, G.R. Purdy, Acta Mater. 61 (2013) 697–707.
[41] L. Carapella, Met. Prog. 46 (1944) 108.
[42] Y.K. Lee, H.C. Shin, D.S. Leem, J.Y. Choi, W. Jin, C.S. Choi, Mater. Sci. Technol. 19 (2003) 393–398.
[43] L. Fan, D. Zhou, T. Wang, S. Li, Q. Wang, Mater. Sci. Eng. A 590 (2014) 224–231.
[44] J.W. Morris, ISIJ Int. 51 (2011) 1569–1575.

[45] C. Wang, M. Wang, J. Shi, W. Hui, H. Dong, Scr. Mater. 58 (2008) 492–495.
[46] R. Ding, Y.J. Yao, B.H. Sun, G. Liu, J.G. He, T. Li, X.H. Wan, Z.B. Dai, D. Ponge, D. Raabe, C. Zhang, A. Godfrey, G. Miyamoto, T. Furuhara, Z.G. Yang, S. van der Zwaag, H. Chen, Sci. Adv. 6 (2020) 1430.
[47] M.M. Wang, C.C. Tasan, D. Ponge, A. Kostka, D. Raabe, Acta Mater. 79 (2014) 268–281.
[48] M. Wiessner, E. Gamsjäger, S. van der Zwaag, P. Angerer, Mater. Sci. Eng. A 682 (2017) 117–125.
[49] E.C. Oliver, P.J. Withers, M.R. Daymond, S. Ueta, T. Mori, Appl. Phys. A-Mater. Sci. Process. 74 (2002) 1143–1145.
[50] T. Matsuno, T. Fujita, T. Matsuda, Y. Shibayama, T. Hojo, I. Watanabe, J. Mater. Process. Technol. 322 (2023) 118174.